This article has been accepted for publication in a future issue of this journal, but has not been fully edited. Content may change prior to final publication. Citation information: DOI 10.1109/TBME.2015.2441636, IEEE Transactions on Biomedical Engineering

The Feasibility of a Smart Surgical Probe for Verification of IRE Treatments Using Electrical Impedance Spectroscopy

Mohammad Bonakdar, *Graduate Student Member, IEEE*, Eduardo L. Latouche, Roop L. Mahajan, *Member, IEEE*, Rafael V. Davalos*, *Member, IEEE*

Abstract*—Significance: Irreversible electroporation (IRE) is gaining popularity as a focal ablation modality for the treatment of unresectable tumors. One clinical limitation of IRE is the absence of methods for real-time treatment evaluation, namely actively monitoring the dimensions of the induced lesion. This information is critical to ensure a complete treatment and minimize collateral damage to the surrounding healthy tissue. Goal: In this study we are taking advantage of the biophysical properties of living tissues to address this critical demand. Methods: Using advanced microfabrication techniques, we have developed an electrical impedance micro-sensor to collect impedance data along the length of a bipolar IRE probe for treatment verification. For probe characterization and interpretation of the readings we used potato tuber, which is a suitable platform for IRE experiments without having the complexities of in vivo or ex vivo models. We used the impedance spectra, along with an electrical model of the tissue, to obtain critical parameters such as the conductivity of the tissue before, during, and after completion of treatment. To validate our results, we used a finite element model to simulate the electric field distribution during treatments in each potato. Results: It is shown that electrical impedance spectroscopy could be used as a technique for treatment verification, and when combined with appropriate FEM modeling can determine the lesion dimensions. Conclusions: This technique has the potential to be readily translated for use with other ablation modalities already being used in clinical settings for the treatment of malignancies.

***Index Terms*—Impedance sensor, Microfabrication, Focal ablation, Electrochemotherapy, Irreversible Electroporation, Ablation monitoring**

I. Introduction

Minimally invasive energy-based focal ablation techniques have received much attention throughout the last few decades, particularly for the treatment of aberrant masses. Radiofrequency ablation (RFA), microwave ablation (MWA), and high-intensity focused ultrasound (HIFU) ablation are among the most commonly used therapies for the management of cancerous tissue [1]. More recently, the phenomenon of electroporation (EP) has opened new windows in the field of focal ablation. Electroporation is a method used to increase the permeability of cell membranes to ions and macromolecules by exposing them to short yet intense pulsed electric fields (PEFs) [2]. Electroporation has been around for decades for *in vitro* applications but it is gaining strength for drug delivery and tumor treatment at the tissue level [3, 4]. During EP a series of short PEFs (70-100 µs) are delivered to the cell population. These pulses affect the transmembrane potential of the cell that can create nano-scale pores on the cell membrane [5]. Depending on the pulse parameters (electric field magnitude, pulse length, number of pulses, etc.), the phenomenon can be either reversible, which is useful for cell transfection, or irreversible, which results in cell death [6]. Therefore, EP gave birth to three treatment modalities: electrochemotherapy (ECT) [7, 8], electro-gene therapy (EGT) [9, 10], and irreversible electroporation (IRE)[11, 12].

Irreversible electroporation (IRE) is a new minimally invasive procedure for the ablation of undesirable tissue [5]. The procedure uses two or more surgical probes (electrodes) to deliver low quantities of energy into the tissue with minimal Joule heating effects and little thermally-induced cell death in the region of interest [13]. IRE lesions typically present sub-millimeter margins between dead and live tissues due to the rapidly decaying electric field surrounding the electrodes [14]. Unlike high-energy thermal-based therapies, IRE spares critical blood vessels and nerves in the periphery as well as the overall stroma surrounding the electrodes [15]. In clinical settings, surgeons have the option to use several imaging techniques such as computer tomography and ultrasound to actively monitor the position of the electrodes in the patient as well as to visualize post-treatment results [16-18].

During any focal ablation therapy, the ability to verify the lesion size is critical [19]. A small lesion may not enclose the whole tumor volume and a large one can damage the surrounding healthy tissue. For most thermal-based tissue ablation mechanisms the created lesions are commonly

Manuscript submitted on February 21, 2015. This study was supported in part by National Science Foundation under the award IIP-1026421 and the Virginia Center for Innovative Technology (CRCF) under award MF13-034-LS.

M. Bonakdar and L. Latouche contributed equally to the production of this work. M. Bonakdar is with the Department of Mechanical Engineering at Virginia Tech, Blacksburg, VA 24060, USA. E. Latouche and *R. Davalos are with the department of Biomedical Engineering and Mechanics at Virginia Tech. 329 Kelly Hall, 325 Stanger St, Blacksburg, VA 24060, USA. (Email: davalos@vt.edu). R. Mahajan is the director of the Institute for Critical Technology and Applied Sciences of Virginia Tech, Blacksburg, VA 24060, USA.

This article has been accepted for publication in a future issue of this journal, but has not been fully edited. Content may change prior to final publication. Citation information: DOI 10.1109/TBME.2015.2441636, IEEE Transactions on Biomedical Engineering

monitored through ultrasound, magnetic resonance, or computer tomography imaging systems, which are not accurate in the description of the area of treatment neither they provide information in an active manner [19]. Although IRE has enjoyed great success in the treatment of inoperable tumors, IRE lesions are moderately hard to predict due to electric field distortion caused by the heterogeneity of most tissues [20]. Currently, treatment planning is performed by finite element models of tissue and electric field distribution with *a priori* information about the tissue of interest to adjust the pulse magnitude for a proper lesion size [6]. Several groups have developed numerical models of electric field distribution during IRE treatment, taking into account the variation of tissue conductivity due to EP and temperature [21-23]. Despite all the advancements in modeling, this method could be challenging when the volume to be treated contains complex heterogeneous structures. In result, some complex tissues such as the pancreas introduce additional challenges, which can lead to high patient to patient variability and result in under-treatment or skip ablations. This highlights the importance of a real-time feedback system for monitoring the progress of the treatment.

Electrical impedance spectroscopy (EIS) has been traditionally used in electrochemical systems for applications such as corrosion monitoring [24], coating evaluation [25] and semiconductor characterization. However in recent years, this method is gaining applications in the characterization of biological systems as a minimally invasive method. These include applications in tissue engineering, cell culture monitoring and disease diagnosis. At the cell level EIS has been used to monitor the electrical properties of single cells [26] and cell cultures in 2D and 3D [27]. Electric cell-substrate impedance spectroscopy (ECIS) is a popular technique for monitoring the growth, motion, integrity and permeability of 2D cell cultures [28, 29].

Recent studies have shown that healthy and cancerous tissues have different dielectric properties [30-32], leading to the application of EIS for cancer diagnosis. EIS could also be applied to the EP-based treatments. EP affects the dielectric properties of cells and tissues due to the alteration in transmembrane pathways and the conductance of the interstitial fluid. Several studies have shown the effect of electroporation on the passive electrical properties of single cells [33-35], cell suspension [36-38], adherent cell cultures [39, 40] and living tissues [41]. These studies have unveiled the potential application of EIS for active monitoring of the lesion during IRE treatments. Some previous studies exist using electrical impedance tomography (EIT) and magnetic resonance electrical impedance tomography (MREIT) to produce an image of the electroporated area *ex vivo* [41-43]. EIT requires the implementation of several electrodes around the treatment zone, which makes it difficult for clinical applications. Ivorra *et al* [44, 45] used plate electrodes to electroporate rat liver *in vivo* and measure the impedance spectrum of the tissue in between the pulses. They found that the conductivity of the liver tissue increases by 9% and 43% after reversible and irreversible electroporation, respectively. Although this method is effective for determining the changes in tissue properties after uniform IRE treatment, it does not provide information about the geometry of the ablated tissue. In general, EIT is difficult to implement because it requires utilizing a large number of external electrodes which must surround the area of interest. MREIT requires no additional electrodes and is not limited to the boundaries of the object of interest, which provides an image with better spatial resolution compared to EIT. However, MREIT adds at least 15 seconds between EP pulses to reconstruct the images making it difficult to use during clinical IRE treatments that commonly utilize 5 times more pulses than EP treatments [43, 46]. Monitoring the conductivity of the tissue during electroporation is also possible by measuring the electric current passing through the tissue during the treatment [47]. This method is easy to implement and less invasive since no additional electrodes are needed for impedance measurement. However, using this method only gives the conductivity of the tissue in the vicinity of the pulsing leads and no information is obtained regarding other areas of the tissue. Although this measurement could provide some insight about the treatment at the point of pulsing, it does not reveal detailed information regarding the geometry of the lesion.

In the last decade, with the advancement of microfabrication techniques, microelectrodes are becoming more available for biomedical applications. These include microelectrode arrays for neural recording and interference [48-52], and electrical impedance micro-sensors for monitoring tissue properties in different situations [53]. Electrical conductivity and thermal conductivity micro-sensors have also been fabricated for the purpose of monitoring tissue properties during RF ablation [54, 55].

In this manuscript we address the feasibility of using a custom-made micro-electrode array along a bipolar IRE probe to actively monitor changes in the impedance of tissue during IRE, and use that information to verify the extent of ablation. The flexible sensor array is made out of biocompatible materials and can be installed on probes of small diameter (~1mm) without causing any constriction during the operation. We have developed a computational model, taking into account the change in the conductivity of the tissue during treatment. This model is used to predict the electric field distribution for different treatment procedures. Measurements taken through our microelecrode-array match the expected results from our computational model, which suggests that the proposed electrode array may be used to verify the expected outcome from treatment planning protocols. We believe that this method can impact the outcome of ablation therapies in the field of surgical oncology by providing surgeons with real-time information about the status of the therapy.

II. Material and Methods

A. Electroporation Setup

To show the principles of sensor operation and be able to use relevant FEM modeling, we had to use an ideal domain for the experiments to factor out parasitic effects which exist in real tissue such as tissue heterogeneity, anisotropy, blood flow and many other factors. For these reasons potato tuber has been chosen as the platform for treatment. Potatoes are a relevant platform and well accepted model for running EP experiments [56-58]. Despite biological differences the main similarity between potato and organs, which makes these experiments

This article has been accepted for publication in a future issue of this journal, but has not been fully edited. Content may change prior to final publication. Citation information: DOI 10.1109/TBME.2015.2441636, IEEE Transactions on Biomedical Engineering

relevant, is that potato cells respond to EP in a similar manner as mammalian cells. That similarity also facilitates the analogy in electrical impedance spectroscopy as potato and tissue share the common equivalent circuit model. The PEFs were generated using an ECM 830 pulse generator (Harvard apparatus, Holliston, MA) and delivered to the tissue through a commercially available IRE bipolar probe (AngioDynamics, Latham, NY). The general geometry of the probe presented a diameter of 1.63 mm with two conductive leads at the tip of 7mm in length each, separated by an 8mm long spacer. Based on clinically established protocols, all the treatments were performed delivering squared pulses of 100μs in length at a repetition rate of 1 pulse per second [14, 59]. Treatments were delivered by applying 10, 30 and 100 pulses of 600, 1000 and 1500 V magnitude to the pulsing leads (total of 9 parameters).

B. Impedance Sensor Fabrication

The fabrication of the micro-sensor array was carried out at the Micro & Nano Fabrication Laboratory at Virginia Tech. A 4" Si wafer was used as the temporary substrate for the fabrication. The wafer was cleaned with acetone, Isopropyl alcohol (IPA) and DI water. Polyimide (PI) solution, PI2525 (HD Microsystems, Parlin NJ) was spin-coated on the Si wafer at 2000 rpm to yield a 13 μm thick PI base layer. To evaporate the solvent, the wafer was soft-baked on a flat hotplate at 120 °C for 30 seconds followed by 150 °C for another 30 seconds. For complete curing of the PI, the wafer was transferred to a furnace. The temperature was ramped up to 200 °C in air environment at a rate of 4 °C/min. After 30 minutes a flow of nitrogen was started at 10 lit/min and the temperature was ramped up to 300 °C. After 1 hour the furnace was turned off and let to cool down to room temperature. Slow heating and cooling rates were necessary to avoid cracking the PI layer. The adhesion between the PI layer and Si wafer is weak, which facilitates detachment of the structure from the wafer after fabrication but could also cause premature detachment in the middle of the fabrication steps. To avoid the later, an adhesion promoter, VM651 (HD Microsystems, Parlin NJ) was used at the edges of the wafer prior to spinning the PI solution to keep the PI layer attached without interfering with the probe structures. A 30 nm thick Cr layer was deposited as an adhesion layer followed by a 100 nm thick gold layer using E-beam evaporation (Kurt Lesker, Clairton PA). The metal layers were photolithographically patterned using AZ9260 positive photoresist (AZ Electronics, Germany) and chemically etched with Cr and gold etchants (Transene, Danvers MA) to form the conductive structures containing bonding pads, wires and sensors. As an insulation, a second layer of PI was spin-coated to 7 μm thickness and cured using the aforementioned technique. The top PI layer on the bonding pads and sensors should be etched down to the gold to expose them. All other PI layers except the designated areas for the probes were etched away to release the individual probes from the wafer. PI dry etching was performed through a titanium mask. 100 nm thick Ti film was deposited and patterned using E-beam evaporation and buffered oxide etch (BOE), respectively. PI etching was performed in oxygen plasma with 30 ml/min oxygen flow rate and 50 W of forward power. Finally, to remove the Ti layer and release the structures, the wafer was dipped into BOE for few seconds. The fabricated sensor was installed on the IRE probe and wires were soldered to the bonding pads. Fig. 1 illustrates the fabrication steps along with the final product.

C. Probe-Sensor Assembly and Calibration

After fabrication, the impedance sensor was installed on the existing IRE probe and connected to the impedance analyzer. The materials and methods developed in this study resulted in a 20 μm thick impedance probe which is thin enough to facilitate its wrapping around the IRE probe without a significant increase in the diameter.

To relate the microsensor readings to the actual conductivity of the medium a calibration experiment was performed. The probe was immersed into salt solutions of known conductivities in the vicinity of the physiological conductivity of tissues, ranging from 2 mS/cm to 20 mS/cm, and the impedance curves were acquired. The resistance was then extracted from the impedance curve by fitting to an appropriate model and a linear regression analysis was performed to find the calibration equation.

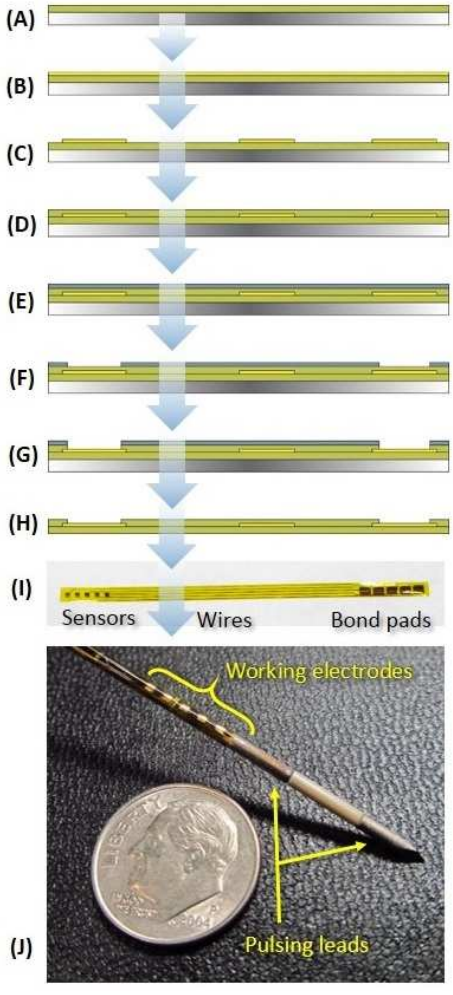

Fig. 1 Probe fabrication steps. (A) Spin polyimide (PI) solution on 4" Si wafer and cure PI (B) Deposit Cr/gold thin film using E-beam evaporation (C) pattern the gold film by photolithography and chemical wet etching to form the electrodes (D) Spin 2nd PI layer and cure.(E) Evaporate titanium thin film (F) Pattern Ti film by photolithography and chemical wet etching to form the mask for dry etching of PI (G) Dry etching of PI layers in oxygen plasma (H) Removing Ti mask and releasing the structure from substrate wafer. (I) Fabricated impedance probe (J) Impedance probe installed on IRE bipolar probe. Size is compared with a dime.

This article has been accepted for publication in a future issue of this journal, but has not been fully edited. Content may change prior to final publication. Citation information: DOI 10.1109/TBME.2015.2441636, IEEE Transactions on Biomedical Engineering

D. Electrical Impedance Spectroscopy (EIS)

The microsensor array is comprised of 5 individual working electrodes (WE) which are located 2.2 mm apart along the probe. The impedance is measured between the consecutive WEs. The chosen electrode placement made it possible to monitor the growth of the lesion up to 1 cm beyond the pulsing leads, which corresponds to clinically relevant lesions when using a bipolar EP probe. The impedance spectrum was measured using a Gamry Reference 600 potentiostat/galvanostat (Gamry, Warminster, PA) in the frequency range of 1Hz-1MHz at ten points per decade. The impedance probe was connected to the impedance analyzer through a custom-made multiplexer which enables switching between different sensors along the probe. The impedance analyzer and the multiplexer were controlled using Gamry Framework 6.12 data acquisition software (Gamry, Warminster, PA). To extract quantitative information about the desired electrical properties of the tissue from the impedance spectrum, it is necessary to fit the spectrum to an equivalent circuit model of the electrode/tissue system. For the best results, the model should contain elements taking into account the effect of electrode/tissue interface, intracellular and extracellular pathways. The Cole-Cole model [60, 61] had been previously used for impedance spectroscopy of tissues during electroporation [44, 62]. In this study the parallel Cole model is adopted with addition of a constant phase element (CPE) to account for electrode-tissue interface (Fig. 2*A*). The CPE is usually described as a capacitance which is frequency dependent with its impedance given by (1):

$$Z = \frac{1}{(jwC)^{\alpha}} \tag{1}$$

where, ω is the angular frequency, j is the imaginary number $\sqrt{-1}$. and C and α are empirical parameters. The α parameter lies between 0.5 and 1, with 1 corresponding to an ideal capacitance. The physical meaning of the CPE is a matter of debate. However α could be regarded as a measure of a distribution of the resistance-capacitance combination and is related to the morphology of the extracellular space [63]. After impedance measurement, the Gamry Echem Analyst software is used to fit the model to the acquired data and get the values for the above parameters.

The Cole-Cole model takes into account the intracellular and extracellular current pathways. Before EP, the cell membrane capacitance prevents the low frequency current from passing through the intracellular space. After EP, the membrane capacitance is shunted by the induced membrane pores, resulting in a lower cell resistance. At tissue level, not all cells undergo EP at the same time, hence instead of a sudden shift in impedance, a transition in impedance spectrum is observed. In this case the parameters R_{ic} and R_{ec} are no longer representative of pure intracellular and extracellular resistivities, but they include the effect of membrane permeabilization as well. However, as previous studies have shown, the Cole-Cole model is still valid for impedance analysis after EP.

E. 1-D IRE Treatments

To characterize the electrical properties of potato in response to EP, and to find the IRE threshold for different number of pulses, a set of 1-dimensional experiments were performed similar to the procedure implemented in [57], in which cylindrical samples of potato are exposed to uniform PEFs between two parallel plate electrodes and the impedance is measured across the same electrodes before and after treatment (see Fig. 2*B*). In addition to that all samples were quantitatively assessed based on the darkening of the sample with respect to its initial color.

Potato tuber tissue was removed using a surgical biopsy needle resulting in cylindrical samples of 6mm in diameter and 5mm in height. Potato samples were exposed to uniform PEFs using parallel aluminum plate electrodes. Connected to the impedance analyzer, the same electrodes were also used for impedance measurements pre- and post-electroporation. A variety of pulse-numbers and magnitude permutations were applied to the samples with $n=4$ for each combination. Resistance values from the impedance measurements were solved for using an equivalent circuit model previously described and used to solve for conductivity of tissue by using (2).

$$R = \frac{L}{A\sigma} \tag{2}$$

where R is the resistance value obtained from impedance measurements, L is the length of the cylindrical sample, A is the cross sectional area of the sample, and σ is the conductivity of the potato.

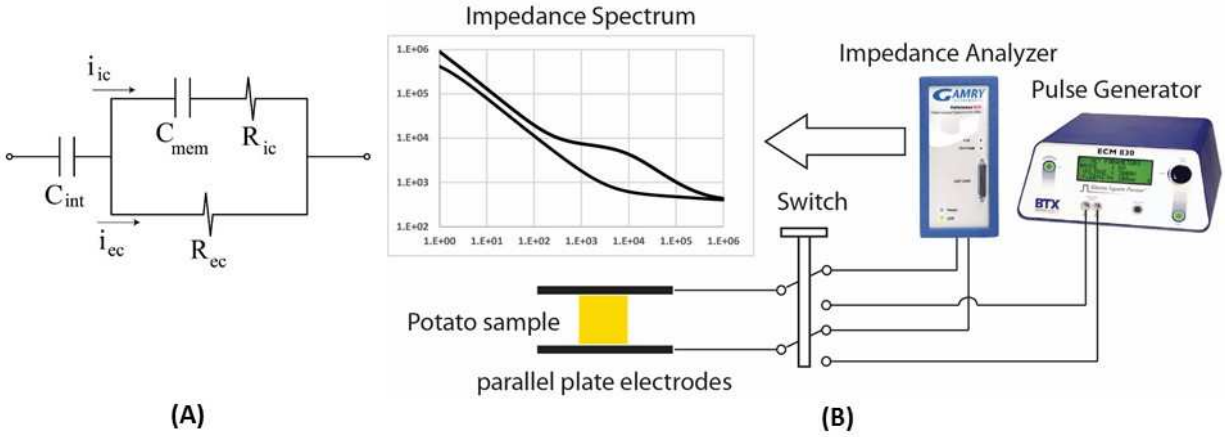

Fig. 2 Impedance measurement and modeling (A) Equivalent circuit model of tissue. (B) Schematic of experimental setup for 1-D IRE response.

This article has been accepted for publication in a future issue of this journal, but has not been fully edited. Content may change prior to final publication. Citation information: DOI 10.1109/TBME.2015.2441636, IEEE Transactions on Biomedical Engineering

In order to assess electroporation, treated samples were stored in petri dishes for 12 hours at which point the samples were placed on a white background and a picture was taken using a digital CCD camera (Canon PowerShot SX110is). All images were converted to grayscale and assessed based on the darkening of the sample with respect to its initial color (control sample) using the ImageJ software (NIH, Bethesda, MD).

F. Derivation of Dynamic Conductivity Function

The results of the 1-D experiments were used to find a model for the variation of conductivity as a function of electric field magnitude and the number of pulses, *i.e.*, $\sigma_d(E)$. For this purpose a sigmoidal equation was developed for each particular number of pulses by fitting to the experimentally obtained conductivity values. Sigmoid functions have been used in the past to describe the change in tissue conductivity due to electroporation [64]. We found that the following equation fits our impedance data very well.

$$\sigma_d = \sigma_0 + a\exp\left(-e^{b(c-E)}\right) \tag{3}$$

In this equation σ_0 is the conductivity of the non-electroporated tissue and E is the applied electric field. The values for parameters a, b, and c were obtained following the best fit of the equation to the experimentally obtained data points for conductivity. Parameter a is the amplitude of the change in conductivity for irreversibly electroporated tissue, b is a constant regulating the growth rate and c is the location of the transition zone.

G. Finite Element Analysis

A finite element model (FEM) was developed in COMSOL Multiphysics® V4.3 (COMSOL, Stockholm, Sweden) to find the electric field distribution inside the tissue for each treatment. A 2-D axisysimmetric platform was used to develop a model that mimics our experimental setup. The geometry used to obtain numerical results was comprised of an ellipsoid with the average dimensions of all treated potatoes along with a simplified geometry of the experimental bipolar probe with both geometries sharing center of mass at the origin. In order to keep the problem general, it was further assumed that the tissue is isotropic and macroscopically homogeneous. The physics involved in solving for the electric field distribution is governed by the following differential equation:

$$\nabla\cdot(\sigma_d\nabla\varphi)=0 \tag{4}$$

where σ_d represents the electrical conductivity of the tissue as described by (3) and φ is the electric potential [6]. Electroporation-induced changes in the conductivity were considered as reported by Neal *et al* [65]. The conductivity range was determined from impedance spectroscopy data collected in 1-D IRE experiments. Boundary conditions for the electrode-tissue interface were set to $\varphi = V_0$ on one electrode while setting the other electrode boundary to $\varphi = 0$. All boundaries with no direct contact with an electrode were assumed thermally and electrically insulative.

Thermal effects during pulsing were modeled by the following Joule heating equation:

$$\nabla\cdot(k_p\nabla T)+\frac{\sigma_d|\nabla\varphi|^2\cdot d}{\tau}=\rho c_p\frac{\partial T}{\partial t} \tag{5}$$

where k_p is the thermal conductivity, T is the temperature, c_p is the specific heat capacity, and ρ is the density of the potato (tissue). The Joule heating term, $\sigma_d|\nabla\varphi|^2\cdot d$, is simplified by using a scale factor directly related to the ratio of pulse duration d, and pulse interval τ. This simplification exemplifies a duty cycle approach in which the total energy delivered to the tissue is averaged throughout the duration of the treatment [66]. IRE is expected to take place in potato tissue exposed to a marginal electric field threshold, which was found by matching experimental lesion dimensions to electric field values from our finite element analysis [57]. A 2D axisymmetric model is used for the FEM analysis. Table I shows the material properties used in making the FEM model.

TABLE I TISSUE PROPERTIES AND CONSTANTS USED IN COMPUTATIONAL MODEL

Material	Property	Symbol	Value	Ref
Potato	Heat capacity, J/(kg·K)	c_p	3033	[67]
	Density, kg/m3	ρ_p	1040	[67]
	Thermal conductivity, W/(m·K)	k_p	0.552	[67]
Electrode	Electrical conductivity, (S/m)	σ_e	2.22E6	[66]
	Heat capacity, J/(kg·K)	c_e	500	[66]
	Density, (kg/m3)	ρ_e	7900	[66]
	Thermal conductivity, W/(m·K)	k_e	15	[66]
Insulation	Electrical conductivity, (S/m)	σ_i	1.0E-5	[66]
	Heat capacity, (J/kg·K)	c_i	3400	[66]
	Density, (kg/m3)	ρ_i	800	[66]
	Thermal conductivity, (W/m·K)	k_i	0.01	[66]

H. Lesion Monitoring During IRE Treatment

The impedance spectrum is measured between consecutive sensors of the impedance probe before and after applying a total number of 10, 30 and 100 pulses for each potato. The impedance spectra before and after pulsing at each sensor are fitted to the equivalent circuit model of Fig. 2*A* to find the circuit parameters. The tissue resistance, R_{ec}, is then converted into the conductivity using the calibration equation. Geometrical factors as well as electrical heterogeneity across different potatoes induce differences in the measured impedance before running any treatment. For this reason the tissue resistances were normalized to their initial values for better comparison.

III. RESULTS

A. Determination of Dynamic Conductivity

Fig. 3 shows the results from the visual inspection of samples after 1-D electroporation experiments. Potato samples exposed to a uniform electric field presented the expected change in coloration when a sufficiently high electric field or number of pulses was delivered. The parallel plate electrodes ensure a uniform electric field across the sample, which results in a uniform treatment. As shown in Fig. 3*A* the color of the treated samples serves as an indication for the occurrence of IRE. The colors of the potato samples were quantitatively analyzed in ImageJ and the normalized contrast with respect to the fully electroporated sample is plotted in Fig. 3*B*.

This article has been accepted for publication in a future issue of this journal, but has not been fully edited. Content may change prior to final publication. Citation information: DOI 10.1109/TBME.2015.2441636, IEEE Transactions on Biomedical Engineering

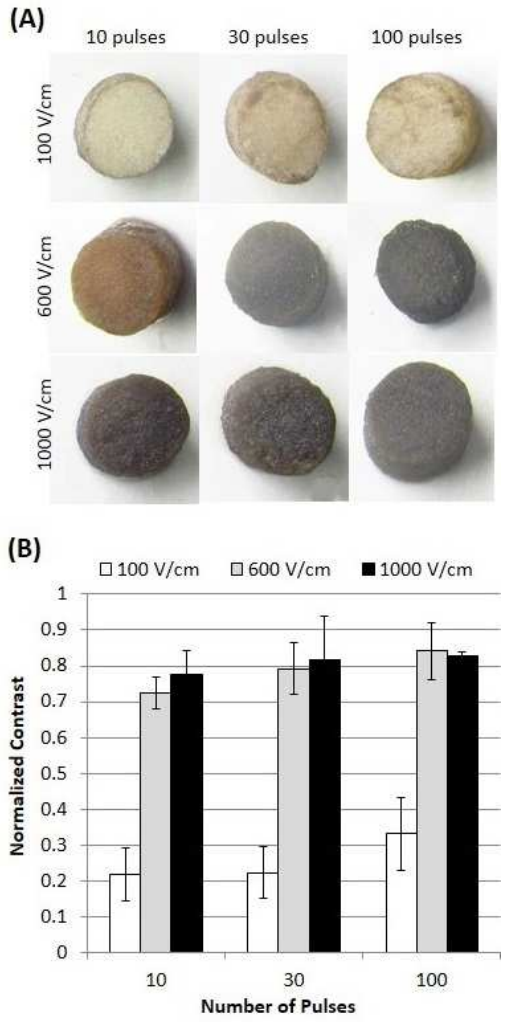

Fig. 3 (A) Potato tuber samples (B) Normalized contrast after 12 hours post-treatment. Data is shown as average ±SD.

The rapid change in the color of potato samples after even a small number of pulses makes it difficult to use the color criterion to find the IRE threshold. It is believed that the electrical conductivity of the tissue increases significantly after IRE treatment. Hence, the increase in the electrical conductivity value is used as the criterion for determination of the IRE threshold.

The shifting in the electrical impedance spectra of potato samples exposed to PEFs of 400 V/cm magnitude and increasing pulse numbers is shown in Fig. 4*A* as an example. For all samples the impedance spectra are analyzed using the equivalent circuit model of Fig. 2*A*. After fitting, the R_{ec} resistance is extracted as a measure of the sample resistance at low frequency [53]. The obtained resistance is then converted to electrical conductivity using (2). The fact that electroporation pulses are short DC pulses justifies using the low frequency electrical conductivity for modeling purposes. Fig. 4*B* shows the data points and the fitted $\sigma_d(E)$ functions as in (3) for 10, 30 and 100 pulses. The inflection point of each curve corresponds to the electric field threshold for the occurrence of electroporation [56, 57], which are found to be 581 V/cm, 298 V/cm, and 227 V/cm for 10 pulses, 30 pulses, and 100 pulses, respectively. The inflection points are shown with hollow circles on the graph.

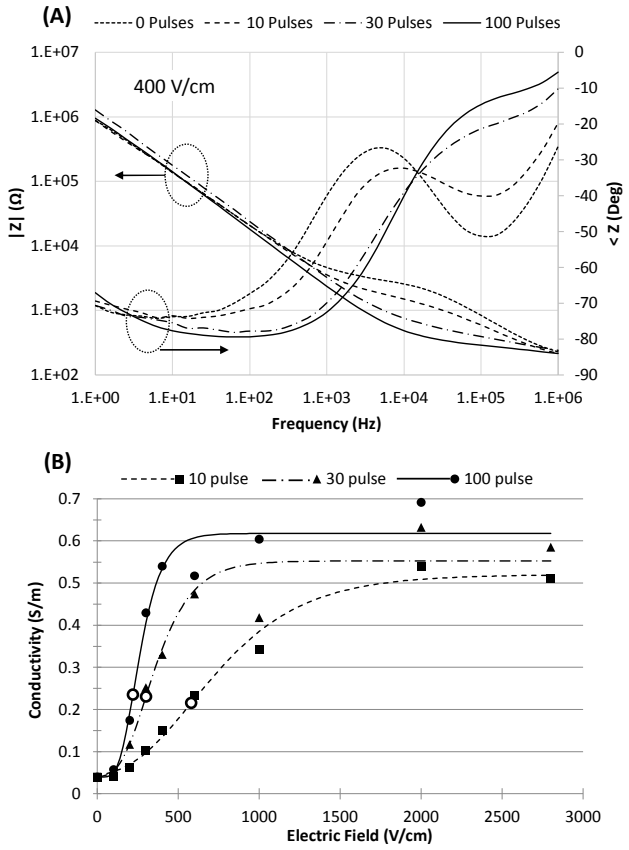

Fig. 4. (A) Comparison of Impedance spectra of potato tuber samples after exposure PEFs of 400V/cm magnitude and increasing number of pulses (B). Electrical conductivity of potato as a function of electric field for different pulse numbers. The inflection points are shown with hollow circles.

B. Electric field distribution from Finite Element Analysis (FEA)

The computational model is solved for 10, 30 and 100 consecutive pulses of 100V, 600V and 1500V to the pulsing leads (total of 9 analyses). Fig. 5 shows the induced electric field magnitude along the length of the IRE probe for each treatment. Generally, the electric field magnitude decreases slightly by increasing the number of applied pulses which is attributed to the increased tissue conductivity during EP treatments as shown in Fig. 4*A*. Each graph also shows the IRE threshold for each number of pulses, as obtained from the dynamic conductivity function. For each number of pulses, the areas of the potato with a higher electric field magnitude than the indicated threshold become irreversibly electroporated. For instance, for 10 pulses of 1500V and 1000V the lesion grows 1.5mm and 0.6mm beyond probe 1, respectively. 10 pulses of 600V will not create any ablation beyond probe 1. By increasing the number of pulses a lower threshold is needed for IRE, as proved by 1-D experiments and shown in Fig. 4*B*. 30 pulses of 1500V, 1000V and 600V will create lesions 3mm, 1.8mm and 0.6mm beyond probe 1.

This article has been accepted for publication in a future issue of this journal, but has not been fully edited. Content may change prior to final publication. Citation information: DOI 10.1109/TBME.2015.2441636, IEEE Transactions on Biomedical Engineering

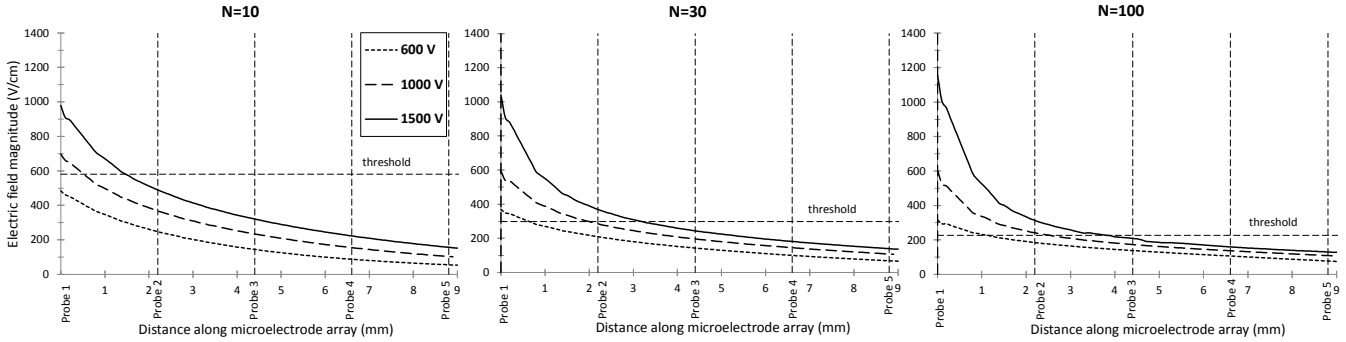

Fig. 5. FEM results for electric field distribution along the length of the probe for different pulse parameters

In this case for 1500V the lesion boundary is located halfway between probe 2 and 3 and for 1000V the lesion is very close to probe 2. For 100 pulses of 1500V, 1000V and 600V, the lesion grows 4mm, 2.5mm and 1mm, respectively, beyond probe 1. In this case for 1500V and 1000V pulses the lesion grow close to probe 3 and probe 2, respectively.

C. Impedance Monitoring During IRE Treatment of Potato

Fig. 6*A* shows the percent change in tissue conductivity between sensor pairs for different treatments. Each diagram shows the change in conductivity after applying a certain number of pulses with different magnitudes. It should be noted that potatoes are heterogeneous and as revealed by our measurements, the conductivity of potato varies up to 24% at different points in different potatoes. Hence, instead of the absolute value of the conductivity, the relative change in tissue conductivity is plotted, which is obtained by normalizing the conductivity after each treatment to the conductivity of bare potato at the same point. As shown in Fig. 6*A*, depending on the applied pulse number and magnitude, certain sensors along the probe undergo a significant increase in the measured electrical conductivity. The results from the 1-D experiments, as shown in Fig. 4*B*, show how a certain increase in electrical conductivity could be related to the occurrence of IRE for the case of homogeneous treatment. However, during the treatment with the bipolar probe, due to the nonuniform electric field, both the ablated and non-ablated areas of the tissue contribute to the impedance measurement, hence a lower increase in electrical conductivity is expected at sensors within the same electric field compared to the 1-D experiment. As shown in Fig. 6*A*, for each number of pulses, the normalized conductivity decreases by moving away from the pulsing leads. This value is equal to 100% (i.e., no increase) for points sufficiently away from the lesion.

Fig. 6*B* shows the induced lesion in potato after 10, 30 and 100 pulses of 1500V. It is shown that for 10 and 30 pulses the lesion edge is located between probes 1&2 and 2&3, respectively. For 100 pulses the lesion has grown up to probe 3. These results are consistent with the FEM results presented in Fig. 5.

IV. DISCUSSION

A. Color of electroporated tissue

As shown in Fig. 3, an acute contrast can be observed between samples exposed to 100V/cm and the rest of the samples. This is in agreement with the data in Fig. 4*B*, as 100V/cm is located below the inflection points of all curves for different number of pulses. The sharp contrast between electroporated and non-electroporated samples is in agreement with the lesions observed inside the treated potatoes as shown in Fig. 6*B*.

B. Interpretation of the impedance spectrum

Based on the equivalent circuit model of Fig. 2*A* the impedance spectrum could be divided into three frequency intervals. At low frequencies (f<1 KHz) the impedance spectrum is dominated by the capacitive behavior of electric double layer at the electrode-tissue interface which is shown by the linearly decreasing impedance magnitude in Fig. 4*A*. At very high frequencies (f>100 KHz) the impedance of all capacitive elements vanish (see (1)), simplifying the equivalent circuit model of Fig. 2*A* to the parallel combination of R_{ic} and R_{ec} as verified by the resistive characteristics of the impedance spectrum at this range. As depicted in Fig. 4*A*, EP does not change the high and low frequency regions of the spectrum. The electric double layer at the electrode interface is not affected by electroporation, resulting in the same capacitance and the same impedance at low frequency range. At high frequency, the cell membrane capacitance is bypassed and the effect of EP on the membrane resistance is not reflected in this part of the spectrum. On the other hand the combination of cytoplasmic and the extracellular resistances which contribute to the high frequency impedance, do not change after EP, resulting in the same impedance at high frequency. At mid frequency range (1 KHz<f<100 KHz) the electrode effects are vanished, however the existing cell membrane capacitance results in part of the intracellular current to pass through the induced membrane pores. Hence, this part of the spectrum is mostly affected by the membrane resistance and undergoes the most significant shift in magnitude after EP due to the decreasing resistance of the cell membrane.

This article has been accepted for publication in a future issue of this journal, but has not been fully edited. Content may change prior to final publication. Citation information: DOI 10.1109/TBME.2015.2441636, IEEE Transactions on Biomedical Engineering

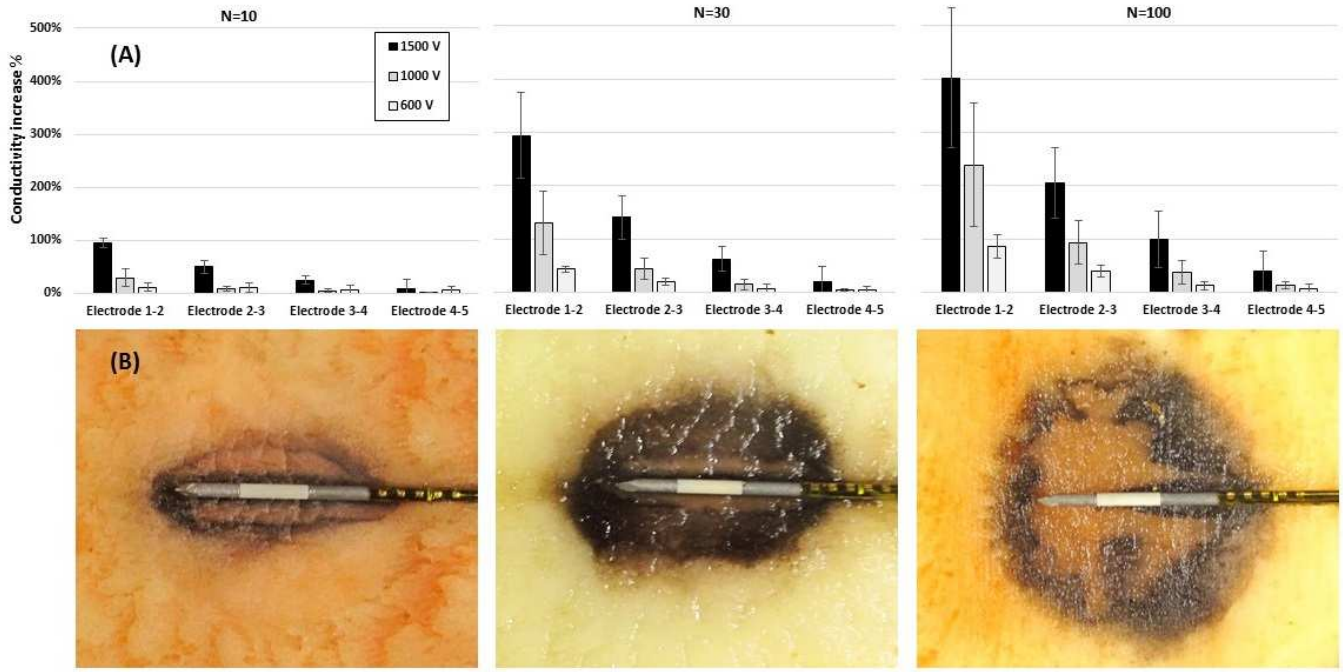

Fig. 6 (A) Change in tissue resistivity at different points along the probe during treatment with different number of pulses (B) The ablated areas inside the potatoes after treating with 10, 30 and 100 pulses of 1500V.

C. Dynamic conductivity function

Fig. 4*B* shows how the electrical conductivity increases after exposure to different pulse numbers of increasing electric field magnitude. It is shown that the transition zone between initial and final conductivity values narrows down as the number of pulses increase, resulting in a sharp increase in electrical conductivity for 100 pulses. But the transition for 10 pulses happens gradually. It should be noted that the inflection points of all three curves correspond to the same conductivity value (~0.22 S/m).

D. Correlation of impedance data and lesion size

As shown in Fig. 6*B*, the lesion starts in an elliptical shape around the pulsing leads of the bipolar probe which further grows into a circular shape after applying sufficient number of pulses (i.e., 100 in this case). This behavior which is confirmed by our FEM modeling, is a result of the change in conductivity after EP.

The impedance data gives feedback about the size of the lesion in both axial and perpendicular directions of the probe. This feedback is quantitative and accurate for determining lesion size in the axial direction yet it allows for qualitative interpretation of lesion growth in the perpendicular direction. In general sensors which are embedded more into the lesion, show a higher increase in the measured conductivity. According to the impedance data and depicted lesions in Fig. 6, sensors which read a doubling in the measured conductivity are located at the lesion boundary along the probe. For example in case of 10 pulses of 1500V, the E12 and E23 measurements show 100% and 50% increase in conductivity, respectively. This means that the lesion has reached E1 but not E2. In case of 30 pulses of 1500V, E23 and E34, measure 150% and 50% increase in conductivity, respectively, which corresponds to the lesion growing up to E2. In case of 100 pulses of 1500V, E34 and E45 measure 100% and 30% increase in conductivity, respectively, which corresponds to the lesion growing close to E4. These measurements are in agreement with the observed lesions in Fig. 6*B* and the predicted lesion size by FEM (Fig. 5).

Lesion growth in the perpendicular direction of the probe is also reflected in the impedance measurement by the probe. For example it is predicted by FEM model (Fig. 5, solid line) and observed in Fig. 6*B* that for 30 and 100 pulse treatments, E1 and E2 would fall within the lesion. However, the corresponding impedance measurement shows 400% and 500% increase in conductivity for 30 and 100 pulses, respectively. This difference is attributed to the depth of the lesion in the perpendicular direction. For the case of 10 pulses of 1500V, the small depth of the lesion in perpendicular direction and the marginal location of E2 compared with the lesion, results in 100% increase in conductivity for E12 measurement. For all treatments, the measurements showing 0% increase in conductivity correspond to electrodes completely outside of the lesion. The results show that the impedance probe is not only capable of monitoring the lesion length along the probe, but also gives relevant information regarding its other dimensions. In this study the correlation of lesion depth and impedance data is shown more qualitatively, however this information when combined with FEM modeling can give accurate shape and size of the lesion in all dimensions.

The FEM model was developed under the assumption of isotropic domains, which is relevant in case of a potato tuber. However some tissues like skeletal muscles are anisotropic, showing different electrical conductivities and IRE thresholds in different directions. This behavior affects the distribution of the electric field within the tissue and consequently the ablated area, as shown in previous studies [68]. However, we believe that, when combined with the proper FEM model, the same

This article has been accepted for publication in a future issue of this journal, but has not been fully edited. Content may change prior to final publication. Citation information: DOI 10.1109/TBME.2015.2441636, IEEE Transactions on Biomedical Engineering

electrode setup could be used for anisotropic tissue as well. This issue is out of the scope of this paper and will be addressed in our future studies.

In our experiments, acquisition of the complete impedance spectrum took about 20 seconds. However, the 10 points per decade resolution of the obtained spectra is far beyond the requirement for fitting the data to the model of Fig. 2*A*. Our results indicate that only a few impedance measurements distributed along the frequency range (depending on the shape of the spectrum) could give us an accurate fitting to the model, reducing the measurement time to a fraction of a second. Therefore, the entire impedance measurement sequence can fit in the inter-pulse time gap of 1 second, facilitating real-time monitoring during the treatment.

E. Possibility of using a passivation layer over the sensor

During the EP experiments in highly conductive medium, it was noted that long treatments with relatively high pulse magnitudes may result in high currents and sparking between the leads. In some instances the sparking resulted in the delamination of the gold from the sensor area close to the pulsing leads. To resolve this issue a 100 nm thick SiO_2 passivation layer was deposited on the sensing area of the impedance probe using E-beam evaporation. The passivation layer acts as a small capacitor which blocks the large DC currents from entering the electrodes and damaging them. The characteristics of this probe is slightly different than the one without the passivation layer due to the existence of the capacitance at the interface, however the overall functionality remains the same. (Data not presented here)

F. Limitations and Sources of error

One of the limitations of the current technique is that the measurements are just taken at one side of the lesion. This is a consequence of the fact that the technique is minimally invasive and no other incision is required into the tissue. In the case of treating homogeneous tissue, a symmetric lesion will be induced and measuring at one side of the IRE leads would suffice for accurate size determination. However, in the case of heterogeneous tissue the induced lesion is not symmetric and the measurements made by the probe will just be valid for one side of the lesion. This is still a useful feedback which could be used for pre-treatment planning verification.

At low EP levels a small error is observed among the measured conductivity values. However the relative error increases at high EP levels which is apparent from the large error bars in Fig. 6*A* for the case of N=100. We noted that during EP treatments, interstitial fluid is forced out of the potato along the length of the probe. This interstitial fluid has a different electrical conductivity than bulk potato tissue and when in contact with the impedance probe may cause some variations in the reading from the actual value, which can lead to large error bars. The temperature increase due to Joule heating happening close to EP leads is also another source of error. We believe the heating effects would be less significant for *in vivo* EP thanks to heat sink effects from blood circulation.

The spatial resolution of the probe for lesion size determination is a function of inter-electrode distance. Generally, the closer the impedance electrodes, the more accurate the measurements become. This parameter can be adjusted and optimized according to the treatment protocol and the expected accuracy.

V. Conclusion

Taking advantage of the characteristic changes in conductivity during irreversible electroporation, we have created a sensor that can be used to collect impedance data during treatments in potato tuber. We performed experiments applying a uniform electric field across cylindrical tissue samples to characterize the IRE thresholds and bulk conductivity changes during treatments. The results from our computational model, which was constructed based on uniform electric field data, correlated well with the lesion dimensions. Using advanced microfabrication techniques, we fabricated a 20μm thick, flexible impedance micro-sensor array. We used impedance data collected through the sensor array to estimate the extent of insult to the tissue for a variety of treatments. Finally, agreement between the FEM and impedance data collected through the sensor array was verified by physically measuring the induced lesion which showed excellent agreement for different protocols.

The system presented herein can be adapted for intra-pulse measurements, which could potentially eliminate overtreatment of tissue and reduce unnecessary thermal effects. Furthermore, the device presented in this study could be readily implemented in the clinic as the proposed micro-sensor is fabricated from biocompatible materials and is relatively easy to manufacture. Finally, this method of active ablation monitoring could potentially be translated for use with other therapies involving probes as energy foci.

Acknowledgment

This study was supported in part by National Science Foundation under the award IIP-1026421 and the Virginia Center for Innovative Technology (CRCF) under award MF13-034-LS. The authors also acknowledge support from Institute for Critical Technology and Applied Science (ICTAS) of Virginia Tech for general support of this research. All authors have patents pending in this technology.

References

[1] K. F. Chu and D. E. Dupuy, "Thermal ablation of tumours: biological mechanisms and advances in therapy," *Nat Rev Cancer*, vol. 14, pp. 199-208, Mar 2014.

[2] A. Ivorra and B. Rubinsky, "Historical Review of Irreversible Electroporation in Medicine," in *Irreversible Electroporation*, B. Rubinsky, Ed., ed: Springer Berlin Heidelberg, 2010, pp. 1-21.

[3] L. M. Mir, *et al.*, "Electrochemotherapy potentiation of antitumour effect of bleomycin by local electric pulses," *Eur J Cancer*, vol. 27, pp. 68-72, 1991.

[4] L. C. Heller and R. Heller, "In vivo electroporation for gene therapy," *Hum Gene Ther*, vol. 17, pp. 890-7, Sep 2006.

[5] R. V. Davalos, *et al.*, "Tissue ablation with irreversible electroporation," *Annals of Biomedical Engineering*, vol. 33, pp. 223-231, Feb 2005.

[6] J. F. Edd and R. V. Davalos, "Mathematical Modeling of irreversible Electroporation for treatment planning," *Technology in Cancer Research & Treatment*, vol. 6, pp. 275-286, Aug 2007.

[7] M. L. Yarmush, *et al.*, "Electroporation-Based Technologies for Medicine: Principles, Applications, and Challenges," *Annual Review of Biomedical Engineering, Vol 16*, vol. 16, pp. 295-320, 2014.

[8] D. Miklavcic, *et al.*, "Electrochemotherapy: from the drawing board into medical practice," *Biomedical Engineering Online*, vol. 13, Mar 12 2014.

[9] D. A. Dean, "Nonviral gene transfer to skeletal, smooth, and cardiac muscle in living animals," *Am J Physiol Cell Physiol*, vol. 289, pp. C233-45, Aug 2005.

[10] M. Jaroszeski, *et al.*, "Delivery of Genes In Vivo Using Pulsed Electric Fields," in *Electrochemotherapy, Electrogenetherapy, and Transdermal Drug Delivery*. vol. 37, M. Jaroszeski, R. Heller, and R. Gilbert, Eds., ed: Humana Press, 2000, pp. 173-186.

[11] C. L. Jiang, *et al.*, "A Review of Basic to Clinical Studies of Irreversible Electroporation Therapy," *Ieee Transactions on Biomedical Engineering*, vol. 62, pp. 4-20, Jan 2015.

[12] H. J. Scheffer, *et al.*, "Irreversible Electroporation for Nonthermal Tumor Ablation in the Clinical Setting: A Systematic Review of Safety and Efficacy," *Journal of Vascular and Interventional Radiology*, vol. 25, pp. 997-1011, Jul 2014.

[13] P. A. Garcia, *et al.*, "Non-Thermal Irreversible Electroporation (N-TIRE) and Adjuvant Fractionated Radiotherapeutic Multimodal Therapy for Intracranial Malignant Glioma in a Canine Patient," *Technology in Cancer Research & Treatment*, vol. 10, pp. 73-83, Feb 2011.

[14] B. Al-Sakere, *et al.*, "Tumor Ablation with Irreversible Electroporation," *Plos One*, vol. 2, Nov 7 2007.

[15] B. Rubinsky, "Irreversible Electroporation in Medicine," *Technology in Cancer Research & Treatment*, vol. 6, pp. 255-259, August 1, 2007 2007.

[16] E. W. Lee, *et al.*, "Imaging guided percutaneous irreversible electroporation: Ultrasound and immunohistological correlation," *Technology in Cancer Research & Treatment*, vol. 6, pp. 287-293, Aug 2007.

[17] B. Rubinsky, *et al.*, "Irreversible electroporation: A new ablation modality - Clinical implications," *Technology in Cancer Research & Treatment*, vol. 6, pp. 37-48, Feb 2007.

[18] E. W. Lee, *et al.*, "Advanced Hepatic Ablation Technique for Creating Complete Cell Death : Irreversible Electroporation," *Radiology*, vol. 255, pp. 426-433, May 2010.

[19] S. N. Goldberg, *et al.*, "Thermal ablation therapy for focal malignancy: a unified approach to underlying principles, techniques, and diagnostic imaging guidance," *AJR Am J Roentgenol*, vol. 174, pp. 323-31, Feb 2000.

[20] C. Daniels and B. Rubinsky, "Electrical Field and Temperature Model of Nonthermal Irreversible Electroporation in Heterogeneous Tissues," *Journal of Biomechanical Engineering-Transactions of the Asme*, vol. 131, Jul 2009.

[21] R. E. Neal, *et al.*, "Experimental Characterization and Numerical Modeling of Tissue Electrical Conductivity during Pulsed Electric Fields for Irreversible Electroporation Treatment Planning," *Ieee Transactions on Biomedical Engineering*, vol. 59, pp. 1076-1085, Apr 2012.

[22] S. Corovic, *et al.*, "In vivo muscle electroporation threshold determination: realistic numerical models and in vivo experiments," *J Membr Biol*, vol. 245, pp. 509-20, Sep 2012.

[23] R. V. Davalos and B. Rubinsky, "Temperature considerations during irreversible electroporation," *International Journal of Heat and Mass Transfer*, vol. 51, pp. 5617-5622, Nov 2008.

[24] Y. Chen and W. P. Jepson, "EIS measurement for corrosion monitoring under multiphase flow conditions," *Electrochimica Acta*, vol. 44, pp. 4453-4464, 7/31/ 1999.

[25] F. Mansfeld and C. H. Tsai, "Determination of Coating Deterioration with EIS: I. Basic Relationships," *Corrosion*, vol. 47, pp. 958-963, 1991/12/01 1991.

[26] T. Sun, *et al.*, "Broadband single cell impedance spectroscopy using maximum length sequences: theoretical analysis and practical considerations," *Measurement Science & Technology*, vol. 18, pp. 2859-2868, Sep 2007.

[27] A. H. Kyle, *et al.*, "Characterization of Three-Dimensional Tissue Cultures Using Electrical Impedance Spectroscopy," *Biophysical Journal*, vol. 76, pp. 2640-2648, 5// 1999.

[28] I. Giaever and C. R. Keese, "Use of Electric Fields to Monitor the Dynamical Aspect of Cell Behavior in Tissue Culture," *Biomedical Engineering, IEEE Transactions on*, vol. BME-33, pp. 242-247, 1986.

[29] C. Tiruppathi, *et al.*, "Electrical method for detection of endothelial cell shape change in real time: assessment of endothelial barrier function," *Proceedings of the National Academy of Sciences*, vol. 89, pp. 7919-7923, September 1, 1992 1992.

[30] J. Estrela da Silva, *et al.*, "Classification of breast tissue by electrical impedance spectroscopy," *Medical and Biological Engineering and Computing*, vol. 38, pp. 26-30, 2000/01/01 2000.

[31] J. Jossinet, "Variability of impedivity in normal and pathological breast tissue," *Medical and Biological Engineering and Computing*, vol. 34, pp. 346-350, 1996/09/01 1996.

[32] S. Laufer, *et al.*, "Electrical impedance characterization of normal and cancerous human hepatic tissue," *Physiol Meas*, vol. 31, pp. 995-1009, Jul 2010.

[33] Y. Huang and B. Rubinsky, "Micro-Electroporation: Improving the Efficiency and Understanding of Electrical Permeabilization of Cells," *Biomedical Microdevices*, vol. 2, pp. 145-150, 1999/03/01 1999.

[34] A. Meir and B. Rubinsky, "Electrical impedance tomographic imaging of a single cell electroporation," *Biomedical Microdevices*, vol. 16, pp. 427-437, 2014/06/01 2014.

[35] R. Davalos, *et al.*, "Electroporation: Bio-electrochemical mass transfer at the nano scale," *Microscale Thermophysical Engineering*, vol. 4, pp. 147-159, 2000.

[36] M. Pavlin, *et al.*, "Effect of Cell Electroporation on the Conductivity of a Cell Suspension," *Biophysical Journal*, vol. 88, pp. 4378-4390, 6// 2005.

[37] J. Zhuang, *et al.*, *Pulsed Electric Field Induced Dielectric Evolution of Mammalian Cells*, 2012.

[38] J. Zhuang, *et al.*, "Dielectric Evolution of Mammalian Cell Membranes after Exposure to Pulsed Electric Fields," *Ieee Transactions on Dielectrics and Electrical Insulation*, vol. 19, pp. 609-622, Apr 2012.

[39] J. A. Stolwijk, *et al.*, "Impedance analysis of adherent cells after in situ electroporation: Non-invasive monitoring during intracellular manipulations," *Biosensors and Bioelectronics*, vol. 26, pp. 4720-4727, 8/15/ 2011.

[40] T. García-Sánchez, *et al.*, "A new spiral microelectrode assembly for electroporation and impedance measurements of adherent cell monolayers," *Biomedical Microdevices*, vol. 16, pp. 575-590, 2014/08/01 2014.

[41] R. V. Davalos, *et al.*, "Electrical impedance tomography for imaging tissue electroporation," *Ieee Transactions on Biomedical Engineering*, vol. 51, pp. 761-767, May 2004.

[42] Y. Granot, *et al.*, "In vivo imaging of irreversible electroporation by means of electrical impedance tomography," *Phys Med Biol*, vol. 54, pp. 4927-4943, Aug 21 2009.

[43] M. Kranjc, *et al.*, "Magnetic resonance electrical impedance tomography for measuring electrical conductivity during electroporation," *Physiological Measurement*, vol. 35, pp. 985-96, Jun 2014.

[44] A. Ivorra and B. Rubinsky, "In vivo electrical impedance measurements during and after electroporation of rat liver," *Bioelectrochemistry*, vol. 70, pp. 287-295, May 2007.

[45] A. Ivorra, *et al.*, "In vivo electrical conductivity measurements during and after tumor electroporation: conductivity changes reflect the treatment outcome," *Phys Med Biol*, vol. 54, pp. 5949-5963, Oct 7 2009.

[46] R. C. G. Martin, "Irreversible Electroporation of Locally Advanced Pancreatic Head Adenocarcinoma," *Journal of Gastrointestinal Surgery*, vol. 17, pp. 1850-1856, Oct 2013.

[47] E. M. Dunki-Jacobs, *et al.*, "Evaluation of Resistance as a Measure of Successful Tumor Ablation During Irreversible Electroporation of the Pancreas," *Journal of the American College of Surgeons*, vol. 218, pp. 179-187, 2// 2014.

[48] Y.-H. Kim, *et al.*, "Robust and real-time monitoring of nerve regeneration using implantable flexible microelectrode array," *Biosensors and Bioelectronics*, vol. 24, pp. 1883-1887, 2009.

[49] P. Norlin, *et al.*, "A 32-site neural recording probe fabricated by DRIE of SOI substrates," *Journal of Micromechanics and Microengineering*, vol. 12, p. 414, 2002.

[50] A. L. Owens, *et al.*, "Multi-electrode array for measuring evoked potentials from surface of ferret primary auditory cortex," *Journal of neuroscience methods*, vol. 58, pp. 209-220, 1995.

[51] I. P. Clements, *et al.*, "Regenerative scaffold electrodes for peripheral nerve interfacing," *Neural Systems and Rehabilitation Engineering, IEEE Transactions on*, vol. 21, pp. 554-566, 2013.

[52] J. Ordonez, *et al.*, "Thin films and microelectrode arrays for neuroprosthetics," *MRS bulletin*, vol. 37, pp. 590-598, 2012.
[53] A. Ivorra, *et al.*, "Minimally invasive silicon probe for electrical impedance measurements in small animals," *Biosensors and bioelectronics*, vol. 19, pp. 391-399, 2003.
[54] Y. Ming, *et al.*, "Micromachined Hot-Wire Thermal Conductivity Probe for Biomedical Applications," *Biomedical Engineering, IEEE Transactions on*, vol. 56, pp. 2477-2484, 2009.
[55] M. Yi, *et al.*, "Micromachined electrical conductivity probe for RF ablation of tumors," in *ASME 2005 International Mechanical Engineering Congress and Exposition*, 2005, pp. 53-56.
[56] R. E. Neal, *et al.*, "Experimental Characterization and Numerical Modeling of Tissue Electrical Conductivity during Pulsed Electric Fields for Irreversible Electroporation Treatment Planning," *Biomedical Engineering, IEEE Transactions on*, vol. 59, pp. 1076-1085, 2012.
[57] A. Ivorra, *et al.*, "Electric Field Redistribution due to Conductivity Changes during Tissue Electroporation: Experiments with a Simple Vegetal Model," *World Congress on Medical Physics and Biomedical Engineering, Vol 25, Pt 13*, vol. 25, pp. 59-62, 2009.
[58] M. Hjouj and B. Rubinsky, "Magnetic Resonance Imaging Characteristics of Nonthermal Irreversible Electroporation in Vegetable Tissue," *The Journal of Membrane Biology*, vol. 236, pp. 137-146, 2010/07/01 2010.
[59] M. Bower, *et al.*, "Irreversible Electroporation of the Pancreas: Definitive Local Therapy Without Systemic Effects," *Journal of Surgical Oncology*, vol. 104, pp. 22-28, Jul 1 2011.
[60] K. S. Cole, "Permeability and impermeability of cell membranes for ions," in *Cold Spring Harbor Symposia on Quantitative Biology*, 1940, pp. 110-122.
[61] O. G. Martinsen and S. Grimnes, *Bioimpedance and bioelectricity basics*: Academic press, 2011.
[62] R. V. Davalos, *et al.*, "A feasibility study for electrical impedance tomography as a means to monitor tissue electroporation for molecular medicine," *Ieee Transactions on Biomedical Engineering*, vol. 49, pp. 400-403, Apr 2002.
[63] A. Ivorra, *et al.*, "Bioimpedance dispersion width as a parameter to monitor living tissues," *Physiological measurement*, vol. 26, p. S165, 2005.
[64] P. A. Garcia, *et al.*, "A Numerical Investigation of the Electric and Thermal Cell Kill Distributions in Electroporation-Based Therapies in Tissue," *Plos One*, vol. 9, Aug 12 2014.
[65] R. E. Neal, 2nd, *et al.*, "In vivo characterization and numerical simulation of prostate properties for non-thermal irreversible electroporation ablation," *Prostate*, vol. 74, pp. 458-68, May 2014.
[66] P. A. Garcia, *et al.*, "A Parametric Study Delineating Irreversible Electroporation from Thermal Damage Based on a Minimally Invasive Intracranial Procedure," *Biomedical Engineering Online*, vol. 10, Apr 30 2011.
[67] M. Rao, J. Barnard, and J. Kenny, "Thermal conductivity and thermal diffusivity of process variety squash and white potatoes.," *Transactions of the ASAE*, 1975.
[68] S. Čorović, *et al.*, "The influence of skeletal muscle anisotropy on electroporation: in vivo study and numerical modeling," *Medical & biological engineering & computing*, vol. 48, pp. 637-648, 2010.

Mohammad Bonakdar (S'15) received the B.S and M.S degrees in Mechanical Engineering from Sharif University of Technology, Tehran, Iran in 2004 and 2007, respectively. He is currently pursuing the Ph.D. degree in Mechanical Engineering at Virginia Tech, Blacksburg, VA, where he has served as research assistant in the Center for Intelligent Materials Systems and Structures (CIMSS) and Bioelectromechanical Systems Laboratory (BEMS). His research interests include bio-MEMS, microfluidics, bio-sensors, electroporation, and organs-on-chip.

Eduardo Latouche received the B.S. degree in Mechanical Engineering from Virginia Tech, VA, USA, in 2013, and is currently working toward the M.S. degree in Engineering Mechanics. After completion of his B.S. degree he joined the Bioelectromechanical Systems Laboratory (BEMS) as a Research Assistant. His research interests include development of medical devices, pulsed electric fields technologies, physics-based therapies, treatment planning, and MEMS.

Roop L. Mahajan received the B.S and M.S degrees in Mechanical Engineering from Punjab Engineering College, India, and the Ph.D. degree in Mechanical Engineering from Cornell University in 1977. He is currently Lewis E. Hester Chair Professor and Director of the Institute for Critical Technology and Applied Science at Virginia Tech where he also concurrently holds a joint appointment as tenured professor in the departments of Mechanical Engineering and Engineering Science Mechanics.

Rafael V. Davalos (M'05) is an Associate Professor and Faculty Fellow in the Virginia Tech – Wake Forest University School of Biomedical Engineering and Sciences. He also holds Adjunct Appointments in Mechanical Engineering, the Wake Forest Comprehensive Cancer Center and at the Wake Forest Institute of Regenerative Medicine. Dr. Davalos received the B.S. degree from Cornell University and the M.S. and Ph.D degrees from the University of California, Berkeley. Prior to his career as a faculty member, Davalos was employed at Sandia National Laboratories and departed as a Principal Member of Technical Staff. Dr. Davalos was the 2006 HENAAC award recipient for the Nation's Most Promising Engineer and received the 2009 award from Virginia Tech College of Engineering for Outstanding Assistant Professor. In 2012 he received the award for the Most Outstanding Dissertation Advisor at Virginia Tech and was recently named a Wallace H. Coulter Fellow.
.